Acta Materialia 152 (2018) 315–326

Contents lists available at ScienceDirect

Acta Materialia

journal homepage: www.elsevier.com/locate/actamat

Full length article

Crystal defect associated selection of phase transformation orientation relationships (ORs)

Meishuai Liu [a, b], Yudong Zhang [b, *], Xinli Wang [c], Benoit Beausir [b], Xiang Zhao [a, **], Liang Zuo [a, d], Claude Esling [b]

[a] Key Laboratory for Anisotropy and Texture of Materials (Ministry of Education), Northeastern University, Shenyang 110819, China
[b] Université de Lorraine, CNRS, Arts et Métiers Paris Tech, LEM3, F-57000 Metz, France
[c] Research Institute, Northeastern University, Shenyang 110819, China
[d] Taiyuan University of Science and Technology, Taiyuan 030024, China

ARTICLE INFO

Article history:
Received 9 February 2018
Received in revised form
10 April 2018
Accepted 13 April 2018
Available online 21 April 2018

Keywords:
Phase transformation
Orientation relationship (OR)
Transformation strain
Deformation gradient tensor
Dislocation

ABSTRACT

Phase transformation in solids always follows specific orientation relationships (ORs). The OR usually ensures a minimum lattice deformation for the structure change. However, in many cases different ORs are respected by the same transformation. The selection role and the link between the OR and the existing crystal defects needs further investigation. Thus, in this work, the α to β heating phase transformation induced by high density Electric Current Pulse (ECP) treatments in an annealed Cu–40%Zn alloy was investigated. Results show that the β phase obeys the K-S OR when formed along the α grain boundaries or in their vicinities, or the N-W OR when formed in the α grain interiors. In the former sites, the $\{111\}_\alpha/\langle 1\bar{1}0\rangle_\alpha$ dislocation arrays were frequently observed, whereas in the latter, the $\{111\}_\alpha/\langle 11\bar{2}\rangle_\alpha$ stacking faults were often found. Transformation strain analyses revealed that under the K-S OR the maximum lattice deformation required is a shear on the $\{111\}_\alpha$ plane in the $\langle 1\bar{1}0\rangle_\alpha$ direction, whereas under the N-W OR the maximum deformation is a shear on the $\{111\}_\alpha$ plane in the $\langle 11\bar{2}\rangle_\alpha$ direction. Thus the existing $\{111\}_\alpha/\langle 1\bar{1}0\rangle_\alpha$ dislocation arrays along the α grain boundaries and in their vicinities provide pre-strain required by the transformation via the K-S path, whereas the $\{111\}_\alpha/\langle 11\bar{2}\rangle_\alpha$ stacking faults boarded by $\{111\}_\alpha/\langle 11\bar{2}\rangle_\alpha$ partial dislocations offer pre-strain facilitating the transformation via the N-W path. The present results provide new information on the role of crystal defects on phase transformation strain path and the selection of transformation ORs.

© 2018 Acta Materialia Inc. Published by Elsevier Ltd. All rights reserved.

1. Introduction

Phase transformations represented by either a pure crystal structure change (displacive) or a crystal structure change accompanied by a chemical composition change (diffusive) from the parent state to the product state happen in many solids when they are subjected to an environmental constraint (thermal, mechanical, magnetic or electric field). In either of the two cases (displacive or diffusive), the structure change is always realized by coordinated atomic movements from the parent crystal structure to the product crystal structure. To ensure that the structure change is energetically economical, a specific orientation relationship (OR) is respected by the two end phases to minimize the lattice distortion energy. Depending on the crystal system of the two end phases, different ORs are present, such as the Kurdjumov-Sachs OR (K-S), i.e., $\{111\}_\alpha//\{110\}_\beta$, $\langle\bar{1}10\rangle_\alpha//\langle\bar{1}11\rangle_\beta$, observed in steels [1–4], Fe–based alloys [5–7] and Cu-Zn alloys [8]; the Nishiyama-Wasserman OR (N-W), i.e., $\{111\}_\alpha//\{110\}_\beta$, $\langle 11\bar{2}\rangle_\alpha//\langle\bar{1}10\rangle_\beta$ in steels [1,3,4], Fe-Ni-Co-Ti shape memory alloy [9] and in Gibeon meteorites [10], the Burgers OR (BOR), i.e., $\{110\}_\beta//\{0001\}_\alpha$, $\langle\bar{1}1\bar{1}\rangle_\beta//\langle 11\bar{2}0\rangle_\alpha$, in Ti based alloys [11–14], the Pitsch OR, i.e., $\{101\}_\alpha//\{12\bar{1}\}_\beta$, $\langle 10\bar{1}\rangle_\alpha//\langle\bar{1}\bar{1}1\rangle_\beta$, in Ni–Mn based intermetallic compounds [15] and other special OR, i.e., $\{001\}_{7M}//\{112\}_{NM}$, $\langle 100\rangle_{7M}//\langle 11\bar{1}\rangle_{NM}$, in Ni–Mn–Ga alloys [16].

The relation between the observed transformation ORs and the possible perfect or partial dislocations to facilitate certain OR variants produced by phase transformation in some materials have

* Corresponding author.
** Corresponding author.
E-mail addresses: meishuai.liu@univ-lorraine.fr (M. Liu), yudong.zhang@univ-lorraine.fr (Y. Zhang), wangxl@mail.neu.edu.cn (X. Wang), benoit.beausir@univ-lorraine.fr (B. Beausir), zhaox@mail.neu.edu.cn (X. Zhao), lzuo@mail.neu.edu.cn (L. Zuo), claude.esling@univ-lorraine.fr (C. Esling).

https://doi.org/10.1016/j.actamat.2018.04.031
1359-6454/© 2018 Acta Materialia Inc. Published by Elsevier Ltd. All rights reserved.

been an interest of study since last century and continues to attract attention [10,17–20] to date. The correspondence relations between the OR plane and the glide plane and between the OR direction and the Burgers vectors of the dislocations (perfect or partial) have been phenomenologically studied for the Kurdjumov-Sachs (K-S) and the Nishiyama-Wassermann (N-W) relations [18,19]. With such an approach of correspondence relations, the association of each plane/burgers vector combination with a particular variant is established and the presence of both "positive slip" and "negative slip" variants within individual grains, a puzzling phenomenon, have been successfully interpreted [18]. The approach explains well the differences in the proportions of the K-S and the N-W variants observed experimentally in relation with the stacking fault energy of the parent phase [18,20]. However, the experimental investigation on the evidences of the corresponding perfect and partial dislocations is further needed, as stated by the authors of [18]. Moreover, the correlation between the strains of the perfect or the partial dislocations and the lattice deformation of the phase transformation to realize the crystal structure change from the parent phase to the product phase needs to be studied to reveal the underlying physical mechanisms of the influence of different types of dislocations on the transformation strain path of different OR variants. Clearly experimental investigations for providing such evidences to correlate the type of dislocations with the transformation OR variants is not easily realizable with the classical cooling phase transformation, as the crystal defects of the parent phase (high temperature phase) cannot be preserved to the convenient observation temperature (room temperature for example) after the phase transformation, unless in-situ TEM observation is performed. However, for in-situ TEM experiments, the localization of the dislocations in the high temperature phase in the observable regions is not controllable, thus the success of the experiments is largely uncertain. Under such a circumstance, heating phase transformation could be a potential alternative if the high temperature phase can be conserved to the room temperature. The types of dislocations in the parent phase can be conveniently investigated before the phase transformation, allowing the correlation with the transformation OR.

In view of such requests, we conducted a thorough crystallographic study on the α to β heating phase transformation in an annealed Cu-40%Zn treated by high density Electric Current Pulse (ECP). The ECP treatment as a special treatment method can realize ultra-rapid heating (the heating rate about 10^6–10^7 K/s) [21] and cooling [21–24] of a bulk material, allowing the conservation of the high temperature phase to the room temperature [25-31] and offering possibility for the investigation of phase transformation. Many studies of ECPed Cu-Zn alloys have demonstrated that the high temperature β phase can be retained to the room temperature [20,28,32–34] and such a β phase maintains an OR of 44.3°<114> [33] close to the K-S OR [34] with the parent α phase. Thus the ECP induced heating phase transformation in annealed Cu-40%Zn alloy provide proper means to effectuate an in-depth study on the impact of the dislocations on the selection of transformation OR and to reveal the physical mechanisms of such selection.

2. Experimental details

The material used in the present work is a hot-rolled Cu-40%Zn sheet (300 × 150 × 1.5 mm). The composition analyzed by the X Ray Fluorescence is given in Table 1 and is very close to the nominal one.

Table 1
Chemical composition (in wt./%) of the hot-rolled Cu-40%Zn alloy.

Cu%	Zn%	Si%
60.86	39.06	<0.01

Dog-bone-shaped samples with gauge dimensions of 10 mm in length, 2 mm in width, and 1.5 mm in thickness, as shown in Fig. 1 (a), were cut out of the center part of the hot-rolled Cu-40%Zn sheet by the electro-spark discharge technique. Then, these samples were heat treated at 773 k in the α+β phase region for 30 min and cooled in air to restore the crystal perfection and to homogenize the microstructure.

The annealed samples were further treated by electric current pulses (ECPs). A schematic illustration of the experimental arrangement is given in Fig. 1 (a). A single electric current pulse was produced by a discharge of the capacitor banks and goes through the annealed samples at room temperature. The two ends of each sample were put into the copper electrodes under atmospheric

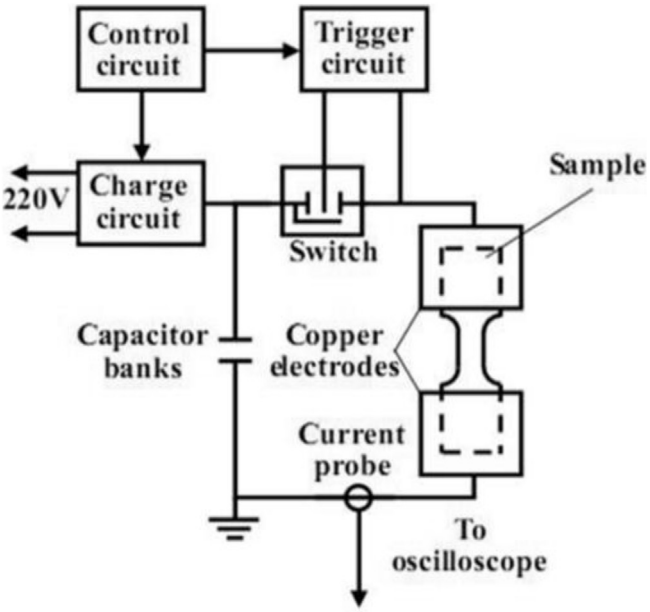

(a)

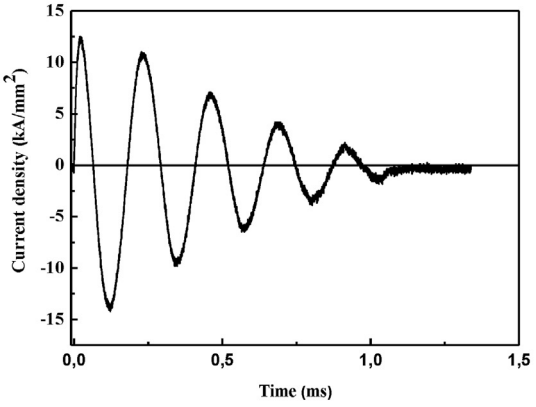

(b)

Fig. 1. (a) Illustration of ECP experimental arrangement. (b) A typical waveform of an ECP.

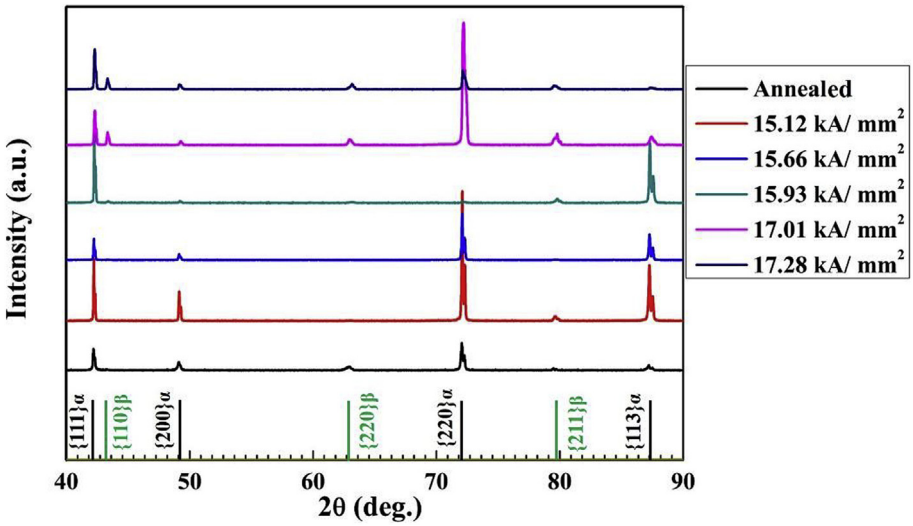

Fig. 2. X-ray diffraction patterns of the annealed and the ECP treated samples. The ideal peak positions of the α and the β phase were indicated with the color lines (black: α phase; green: β phase) at the bottom of the figure. (For interpretation of the references to color in this figure legend, the reader is referred to the Web version of this article.)

condition during the ECP treatment. Fig. 1 (b) displays a typical wave profile of an electric current pulse. The pulse takes a form of a damped oscillation wave. During the treatment, the instantaneous maximum current density and the pulse remaining time were recorded using a Rogowski coil and a TDS3012 digital storage oscilloscope (Tektronix, Beaverton, Oregon).

In this work, the ECP treatment was performed at various instant electric voltages that correspond to the current densities of about 15.12 kA/mm^2, 15.66 kA/mm^2, 15.93 kA/mm^2, 17.01 kA/mm^2 and 17.28 kA/mm^2, respectively, with the pulse duration of 117 μs, 118 μs, 125 μs, 150 μs and 150 μs.

The phase constituents and their lattice constants of the samples before and after the ECP treatments were analyzed by X-ray diffraction (XRD, Rigaku, Smartlab), using a Cu-Kα radiation at room temperature. The diffraction patterns were measured at a 2θ range from 40° to 90°. The "step" mode was used with a scanning step of 0.01° (2θ) and a duration of 4 s. The software Jana 2006 was used to determine the lattice constants.

The microstructural examinations and crystallographic orientation investigations were performed in a field emission gun scanning electron microscope (SEM, Jeol JSM 6500 F) with an EBSD acquisition camera and the Aztec online acquisition software package (Oxford Instruments). During the EBSD measurements, the "beam-control" mode was used with a step size of 0.15 μm under an accelerating voltage of 15 kV. The EBSD data were analyzed with the Channel 5 software (Oxford Instruments) and the Atex software [35]. The EBSD samples were first mechanically ground using the emery/SiC grinding paper up to 5 μm and then polished using diamond paste (1 μm), and then electrolytically polished with a solution of 20% (volume fraction) nitride acid in methanol at 18 V for 3 s at room temperature.

The nano scaled microstructural and crystallographic features of the constituent phases were analyzed using a Philips CM 200 transmission electron microscope (TEM) operated at 200 kV. The TEM is equipped with a LaB6 cathode, a Gatan Orius 833 CCD camera, and homemade automatic orientation analysis software – Euclid's Phantasies (EP) [36,37]. TEM thin films were prepared first by mechanical thinning to 80 μm in thickness and then by electro polishing to perforation at −34 °C with a solution of 20% (volume fraction) nitride acid in methanol at a voltage of 18 V, using a Struers Tenupol-5 twin-jet electropolisher.

During TEM examination, the dislocation types and the dislocation Burgers vectors were analyzed by matching the observed dislocation line orientation with the theoretical ones as described in [38]. The atomic correspondences for the structure transformation from the parent α phase to the product β phase were analyzed using the Crystal Maker® [39] software.

3. Results

3.1. Phase constituents and lattice constants

Fig. 2 displays the X-ray diffraction patterns of the samples before and after the ECP treatments. It should be mentioned that as the patterns were measured from the bulk samples, the intensities of the peaks are strongly affected by the local texture of the measured regions, thus the corresponding peak intensities from sample to sample change. It is seen from the patterns that all the samples contain two phases (FCC α and BCC β). With the peak positions, the lattice constants of the two phases in the samples without and with the ECP treatments were calculated and listed in Table 2. It is seen that the lattice constants of the two phases change very slightly with the ECP treatment. Those of the α phase decrease with the increase of the current density, whereas those of the β phase decrease first from the initial state and then increase with the increase of the current density. These measured lattice constants of the parent and the product phases allow accurate analyses of the lattice strains for the phase transformation induced by the ECP, as demonstrated later.

Table 2
Lattice constants of α and β phase in the annealed and in the ECP treated samples.

Electric Current Density (kA/mm^2)	α	β
0	3.702612	2.951775
15.12	3.703542	2.921082
15.66	3.701506	2.928865
15.93	3.701626	2.944449
17.01	3.698314	2.948694
17.28	3.699182	2.950145

3.2. Microstructure evolution

3.2.1. Annealed microstructure

Fig. 3 (a) and (b) show the EBSD micrographs of the annealed Cu-40%Zn alloy, where the β phase is in blue and the α phase in gray (EBSD band quality index contrast). It can be seen that the annealed microstructure is mainly composed of α phase (about 96.21%) with equiaxed grain shape. The β phase is much less in quantity (about 3.79%) and located at the α grain boundaries and triple-junctions, forming bands along the previous hot rolling direction, as shown in Fig. 3 (a). Within the α grains there are always long and straight Σ3 (<111>60°) boundaries, as outlined in red in Fig. 3 (b). This indicates that the α grains contain {111}<11$\bar{2}$> twins as two FCC crystals possessing a disorientation of 60° around the <111> axis is {111} <11$\bar{2}$> twin related. Occasionally, curved Σ3 boundaries appear as grain boundaries. According to the coincidence with the {111} twinning plane K_1, these Σ3 boundaries can be further classified into two types. Hereafter we denote those coincident with the K_1 plane GB_{K_1} boundaries and those not coincident with the K_1 plane non-K_1-Σ3 grain boundaries GB_{non-K_1}, as indicated in Fig. 3 (b).

TEM examinations revealed that the annealed α matrix possesses two kinds of crystal defects located on α grain boundaries and in α grain interiors. Although the two kinds of defects are not numerous, their occurrence is certain. The one is parallel dislocation arrays that are mainly located on α grain boundaries, as shown with a typical example in Fig. 4 (a) and very occasionally located in the vicinities of α grain boundaries, as shown in Fig. 4 (b). Further analysis demonstrated that such dislocations are mainly of <1$\bar{1}$0> $\{111\}_\alpha$ edge type. The other type of defects is stacking faults, as shown with a typical example in Fig. 4 (c). Trace analysis of the stacking faults confirmed that they are of <11$\bar{2}$>$\{111\}_\alpha$ type that is typical for FCC low stacking fault metals, such as the α phase of the present alloy. This kind of stacking faults evidences the existence of the <11$\bar{2}$>$\{111\}_\alpha$ partial dislocations that are located along the boundaries between the faulted and non-faulted regions.

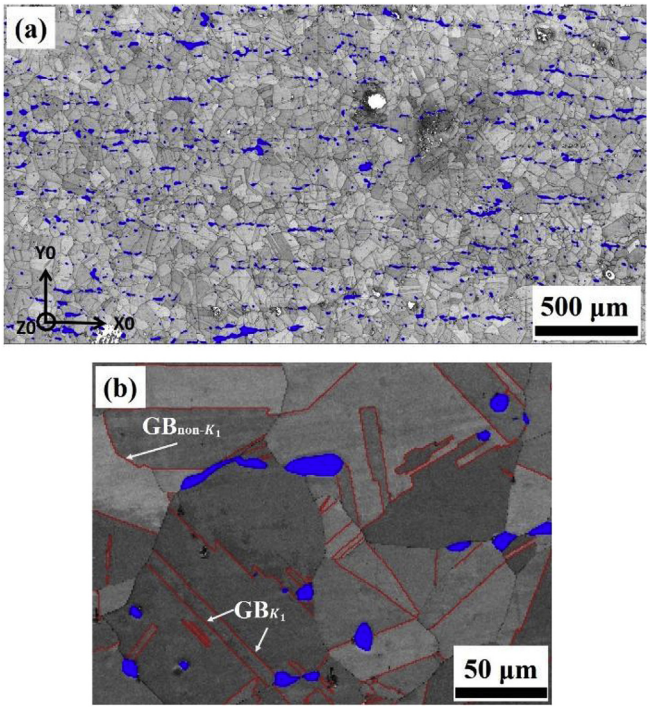

Fig. 3. (a) and (b) SEM-EBSD micrographs of annealed Cu-40%Zn alloy, where the β phase is in blue whereas the α phase is in gray represented with its EBSD band quality index contrast, and Σ3 boundaries are in red (b). (For interpretation of the references to color in this figure legend, the reader is referred to the Web version of this article.)

3.2.2. Microstructure after ECP treatment

Fig. 5 shows the EBSD micrographs of the Cu-40%Zn alloy after ECP treatments, where the α grains are in gray represented with the EBSD band quality index contrast and the β ones are in color according to their crystallographic orientations. Comparing with the annealed sample (Fig. 2 (b)), one can find that some fine β precipitates appear in the α phase. The amount of the precipitates increases with the increase of the electric current density, from 0.64% at 15.12 kA/mm^2 to 11.5% at 17.28 kA/mm^2. With the increase of the amount of the β precipitates, the formation sites of the β precipitates also increases, from the random high angle (>10°) α grain boundaries (as indicated in the insert of Fig. 5 (a) and (b)) at low current density, to the non-K_1-Σ3 boundaries (as indicated in the insert of Fig. 5 (c)) and the α grain interiors (Fig. 5 (c) to (e)), and then to the K_1-Σ3 boundaries (as indicated in the insert of Fig. 5 (d)) at the high current density. Here we denote the β precipitates at the α random high angle boundaries β_{HGB}, those at GB_{non-K_1} boundaries β_{non-K_1}, those at GB_{K_1} boundaries β_{K_1} and those at α grain interiors β_{GI}. Such a nucleation sequence from low current to high current density demonstrates that the α grain boundaries are the preferred formation sites for the β precipitates, especially the high angle and non-coherent boundaries.

In addition to the precipitation of the β phase during the ECP treatments, the initial β grains tend to transform to α phase when the current density reached 17.01 kA/mm^2 (Fig. 5 (d) and (e)). In the present work, as we only focus on the α to β transformation, the β to α transformation will not be included in the later sections.

3.2.3. Orientation relationship (OR) between α/β

By crystallographic analyses, using the measured orientations of the parent α phase and the β precipitates, we found that one part of β precipitates respects the N-W with the surrounding α phase, whereas the other part respects the K-S ORs with the neighboring α phase, both with certain angular deviations (up to 5°), as shown in Fig. 6 (a) and (b), where the colored contour lines around the β precipitates indicate the angular deviations from the exact OR. The plane and direction parallelisms of the respective K-S and the N-W ORs are illustrated in the corresponding plane and direction pole figures in Fig. 6 (c) and (d), using the example orientation data of the two phase measured by EBSD.

Table 3 shows the detailed results the OR and the corresponding angular deviations from the exact OR of the β precipitates obtained from the examination of a large number of randomly selected β precipitates along the α grain boundaries (β_{GB}) and in the α grain interiors (β_{GI}) under the ECP treatments. To visualize the different populations of the β precipitates with respect to the two ORs, the deviations of all the selected β precipitates from the ideal N-W OR (equivalent to a 45.98° rotation around the <0.976 0.083 0.201 > axis) and also from the ideal K-S OR (equivalent to a 42.85° rotation around the <0.968 0.178 0.178 > axis) are presented in histograms and displayed in Fig. 7. It should be noted that both the deviations from the rotation angle and the rotation axis are considered. It is seen from Table 3 and Fig. 7 that most β_{GB} respects the K-S OR whereas the most β_{GI} obeys the N-W OR. In addition, the β_{GI} obeying the K-S OR are located in the vicinities of the α grain boundaries. These results demonstrate that the transformation OR of the β precipitates induced by the ECP is rather selective, depending on the formation location. As at these sites we found different types of dislocations, the selection of the OR should be related to the specific dislocations.

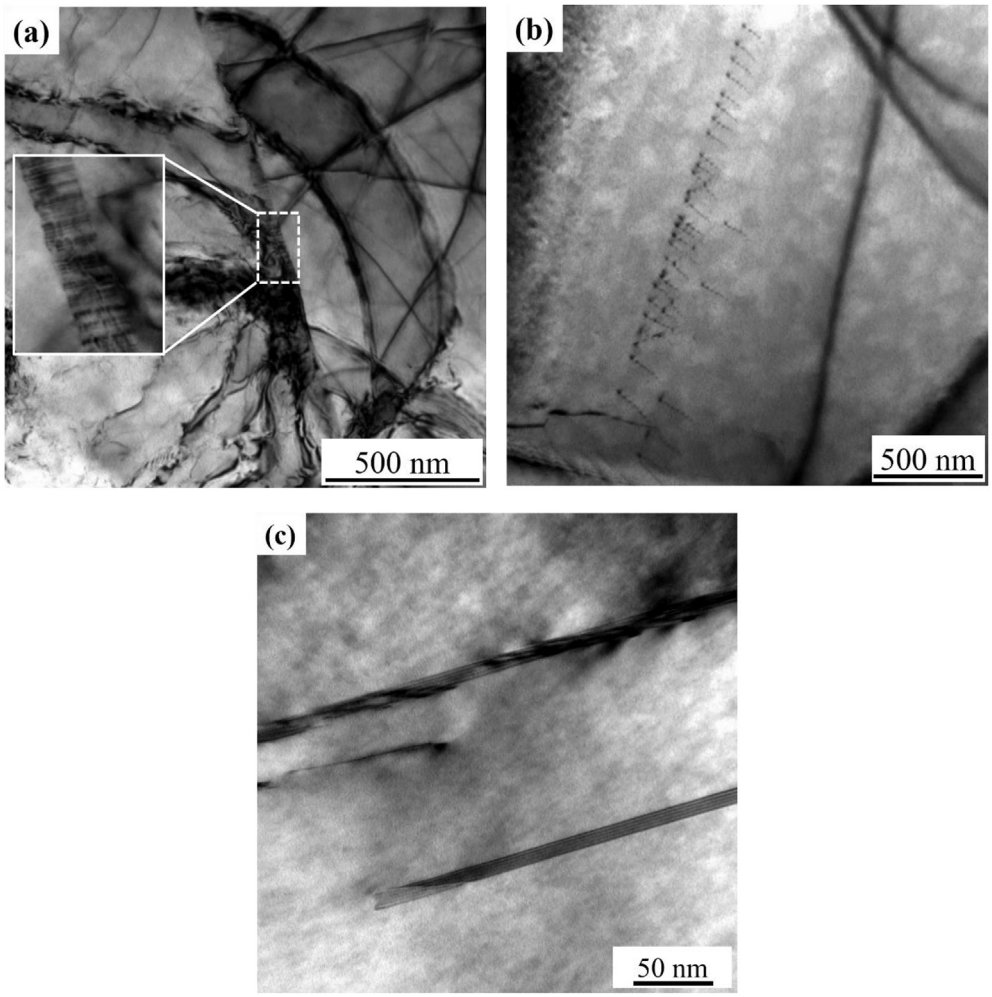

Fig. 4. TEM bright field micrographs of two kinds of crystal defects on α grain boundaries and in α grain interiors. (a) and (b) dislocation arrays and (c) stacking faults.

3.2.4. Morphology of intragranular β (β_{GI})

Here, we mainly focus on the morphologies of the intragranular β (β_{GI}) precipitates. From large scaled microstructure examinations (not shown here), we found that the β_{GI} precipitates are monolithic in bar shape as shown in Fig. 5. By statistical trace analysis, we further found that the precipitates are encased in two pairs of parallel planes, $\{211\}_\alpha$ and $\{311\}_\alpha$ of α phase as the prismatic planes. These planes correspond to the respective $\{112\}_\beta$ and $\{21\bar{1}\}_\beta$ (or $\{12\bar{1}\}_\beta$) planes of the β phase, as shown with the corresponding pole figures of the example β_{GI} precipitates in Fig. 8. In the figures, the microstructures of the β_{GI} precipitates are displayed in colors according to their crystallographic orientations. The surfaces of the precipitates are illustrated with the dashed lines and the traces the solid lines in the consistent colors. The corresponding poles of the surface planes are indicated with the circles. According to the orientation of the parallel directions from the two phases ($<112>_\alpha$// $<111>_\beta$) under the N-W transformation OR, *i.e.*, the OR direction, enclosed in the black boxes in Fig. 8, with respect to the surface planes $\{311\}_\alpha$ and $\{211\}_\alpha$, the β_{GI} precipitates are further classified into three types referred to as precipitate A, B and C, as illustrated in Fig. 8. The geometrical relations between the surface planes and the OR direction of the three types of β_{GI} are summarized in Table 4.

For Type A, the precipitates are in long bar shape and the N-W OR direction ($<112>_\alpha$) is nearly parallel to the two pairs of surface planes. For Type B, the length of the bars is much shorter. The OR direction is nearly parallel to one pair of the surface plane ($\{211\}_\alpha$) but largely deviated from the other pair ($\{311\}_\alpha$). For Type C, the shape is not regular and the OR direction is not fixed with respect to the two pairs of surface planes. It changes from one case to another. The occurrences of the three types of precipitates are also different under different current densities, as displayed in Table 5. Type A is in absolute majority and the other two are in minority. However, with the increase of the current density the occurrence of Type A decreases. It should be mentioned that with the increase of the current density, the number and sizes of β_{GI} drastically increased and the precipitates formed all over the parent α grains. Thus the lattice of the parent grains should be largely distorted due to the lattice mismatch between the two phases (the lattice deformation will be detailed later). The lattice distortions should impose constraints on the elongation of the precipitates. This suggests that the preferred elongation direction of the β precipitates is close to the OR direction.

4. Discussion

Under the condition of the present initial microstructure of the

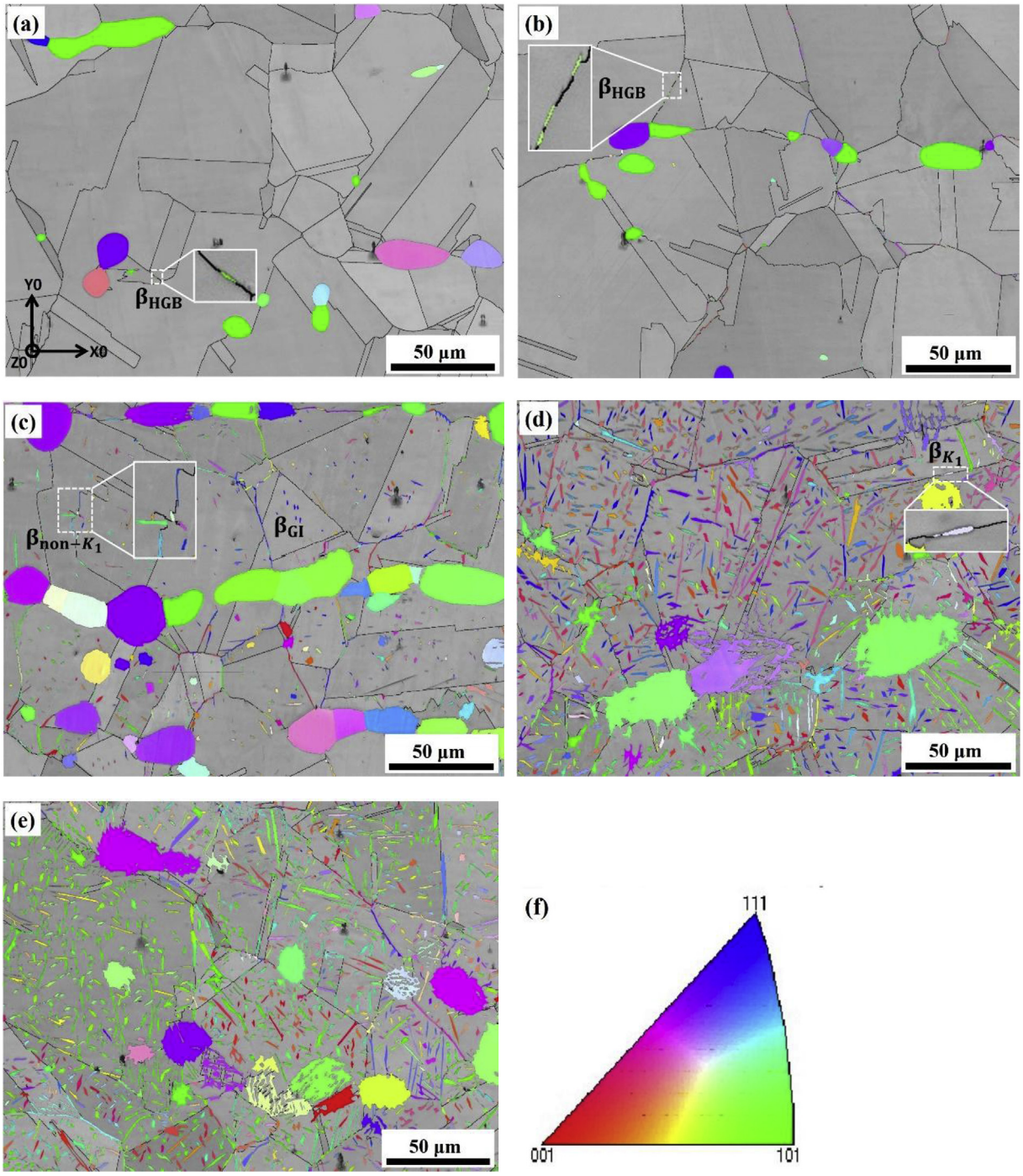

Fig. 5. SEM-EBSD micrographs of Cu-40%Zn alloy after ECP treatments where the α grains are in gray according to the EBSD band quality indices and the β phase in color according to its crystallographic orientation with respect to the X0 axis (X0 inverse pole figure (IPF) micrograph). (a) The ECP density $j_{max} = 15.12$ kA/mm^2 (b) $j_{max} = 15.66$ kA/mm^2 (c) $j_{max} = 15.93$ kA/mm^2 (d) $j_{max} = 17.01$ kA/mm^2 (e) $j_{max} = 17.28$ kA/mm^2 and (f) the X0 IPF color code. The electric current direction is in the X0 direction. (For interpretation of the references to color in this figure legend, the reader is referred to the Web version of this article.)

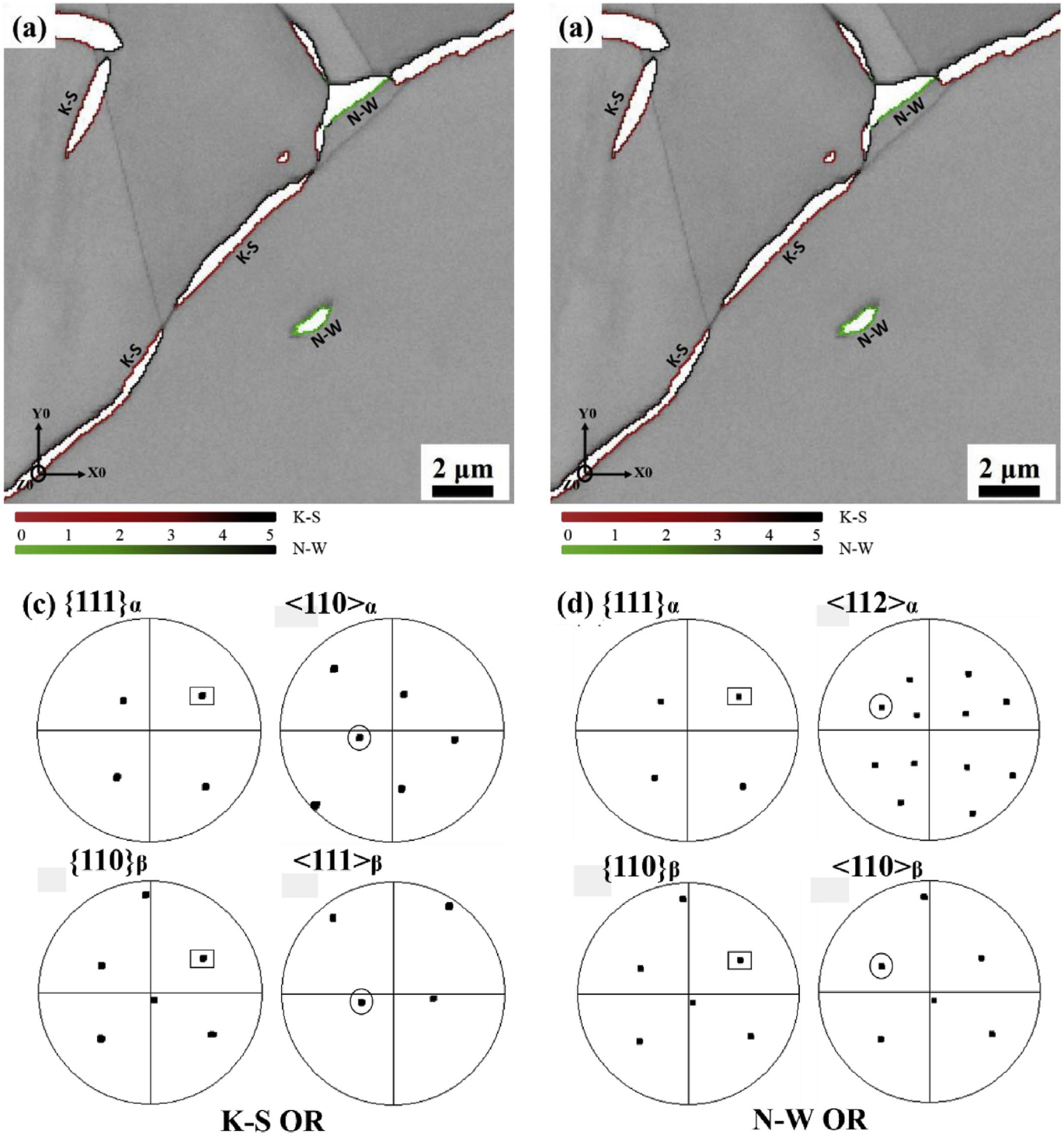

Fig. 6. SEM-EBSD micrograph of α and β precipitates in Cu-40%Zn alloy after ECP treatment. The α grains are in gray contrasted with the EBSD band quality indices and the β ones are in white. The colored contour lines around the β precipitates indicate the angular deviations from the exact OR. (a) β_{GB} along α grain boundaries, (b) β_{GI} in α grain interiors and (c) and (d) corresponding OR direction and plane pole figures of the parent α and the β precipitates obeying the K-S OR and the N-W OR, respectively. The overlapped poles are indicated with the rectangles (plane) and the circles (direction).

Table 3
β/α phase boundary length fractions of β_{GB} and β_{GI} that obey different transformation ORs (the K-S: 42.85°/< 0.968 0.178 0.178 > and the N-W: 45.98°/< 0.976 0.083 0.201 >) at different deviation ranges (from both the rotation angle and the rotation axis) from the exact OR, obtained under different ECP treatments. For the β_{GI}, the statistics were counted from about 500 precipitates at 15.93 kA/mm^2 to 2000 precipitates at 17.28 kA/mm^2 and for the β_{GB}, the statistics were collected from around 600 precipitates.

	Electric Current Density (kA/mm^2)	OR	0-3°	3-7°
α/β_{GI}	15.93	K-S	38.2%	1.1%
		N-W	60.7%	
	17.01	K-S	28.4%	0.5%
		N-W	71.1%	
	17.28	K-S	31.8%	0.4%
		N-W	67.8%	
α/β_{GB}	15.66	K-S	76.2%	1.3%
		N-W	22.5%	
	15.93	K-S	78.6%	0.9%
		N-W	20.5%	
	17.01	K-S	73.3%	0.6%
		N-W	26.1%	
	17.28	K-S	60.1%	1.1%
		N-W	38.8%	

Cu-40%Zn alloy, the transformation OR of the β precipitates formed under the present ECP treatments are characteristic depending on the formation location. On the α grain boundaries, the OR is mostly the K-S, whereas in the α grain interiors, the OR is mostly the N-W, suggesting that the lattice distortion to realize the structure transformation from the α phase to the β phase proceeds in different ways and makes use of different crystal defects. The different transformation ORs may represent different lattice strain paths for the structure transformation. To further explore the transformation deformation, the lattice strains to form the β precipitates having a BCC structure from the α phase with an FCC structure under the two ORs (K-S and N-W) were analyzed using the lattice constants determined from the XRD diffraction measurements (Table 2) and represented with the deformation gradient tensor **A** [33] expressed in the corresponding OR reference systems. Fig. 9 shows the lattice correspondences of the two phases under the two ORs and the OR reference systems (***i-j-k***). For each OR reference system, ***j*** is set parallel to OR direction, ***k*** to the direction normal to the OR plane and ***i*** to the vector product of ***j*** and ***k***. A general form of the deformation gradient tensor is given in Eq. (1), where the diagonal element in the tensor a_{ii} ($i = 1$, 2 and 3) represents an elongation ($a_{ii} > 1$) or a contraction ($a_{ii} < 1$) in the direction of ***i*** when the lattice change from α to β, whereas the off diagonal element a_{ij} (i and $j = 1$, 2 and 3), represents a shear in the direction of ***i*** and on the plane normal to ***j***.

$$A = \begin{bmatrix} a_{11} & a_{12} & a_{13} \\ a_{21} & a_{22} & a_{23} \\ a_{31} & a_{32} & a_{33} \end{bmatrix} \quad (1)$$

The tensors obtained by examining the lattice correspondences of the two phases under the two ORs, using the measured lattice constants of the two phases in the sample treated at 17.28 kA/mm^2 as examples are given in Table 6.

It is seen that for the formation of the K-S β phase it requires an elongation of 0.0634 in the $[\bar{1}\bar{1}2]_\alpha$ direction (a_{11}) of the α lattice, a contraction of 0.0233 in the $[1\bar{1}0]_\alpha$ direction (a_{22}) and in the $[111]_\alpha$ direction (a_{33}). The transformation also requires three shear deformations, a shear of 0.1880 on the $(111)_\alpha$ plane and in the $[\bar{1}\bar{1}2]_\alpha$ direction (a_{13}), a shear of −0.1880 on the $(\bar{1}\bar{1}2)_\alpha$ plane and in the $[1\bar{1}0]_\alpha$ direction (a_{21}) and a shear of 0.2658 on the $(111)_\alpha$ plane and in the $[1\bar{1}0]_\alpha$ direction (a_{23}), as shown in Table 6. Clearly the shear strains are much larger than those of the normal strains. Among the three shear strains, a_{23} is the largest. It should be noted that the shear system of a_{23} corresponds to the $\{111\}_\alpha/<1\bar{1}0>_\alpha$ slip system of FCC crystals, thus the existing $\{111\}_\alpha/<1\bar{1}0>_\alpha$ dislocation arrays found along the α grain boundaries should facilitate the structure transformation from the α phase to the β phase via the K-S path.

For the N-W β precipitates, the transformation requires the α lattice to elongate by 0.1279 in the $[1\bar{1}0]_\alpha$ direction (a_{11}), to contract by 0.0791 in the $[11\bar{2}]_\alpha$ direction (a_{22}), to contract by 0.0233 in the $[111]_\alpha$ direction (a_{33}) and to shear by 0.3256 on the $(111)_\alpha$ plane and in the $[11\bar{2}]_\alpha$ direction (a_{23}), as shown in Table 6. Also the shear deformation is much larger than the normal strains under the N-W path. Interestingly, the required shear system is $\{111\}_\alpha/<11\bar{2}>_\alpha$ that corresponds to the partial slip system of FCC crystals. It is known that Cu-40%Zn has relatively low stack fault energy. Stacking faults are one of the important crystal defects in this alloy, as observed in the α grain interiors in the present work. Thus, the existing $\{111\}_\alpha/<11\bar{2}>_\alpha$ stacking faults should be favorable for the formation of β precipitates via the N-W path. In consequence, the existence of different dislocations in different locations in the as annealed Cu-40%Zn provide different pre-strain to facilitate the transformation via different strain paths and are at the origin of the selection of the transformation OR.

The morphology of the β precipitates obeying the N-W OR in the α grain interiors is also related to the characteristic lattice strain. As the shear deformation $\{111\}_\alpha/<11\bar{2}>_\alpha$ is the major lattice strain, the elongation of the N-W β precipitates in the shear direction generates less accumulated lattice distortion in the transformation front than the thickening of the precipitates in the directions perpendicular to the shear direction. Thus the shear deformation restricts the thickening of the β precipitates and facilitates the elongation of the β precipitates along the shear direction during the growth process. However, such ideal morphology should be obtained at the beginning of the transformation when the matrix is distortion free. With the increase of the current densities or the prolongation of the transformation, the remaining α matrix becomes distorted due to the formation of the early β precipitates thus the growth of the newly formed β precipitates deviates from the low distortion growth direction in the stress free medium and the morphology changes.

5. Summary

In the present work, the crystallographic features of the phase transformation from the low temperature α phase to the high temperature β phase induced by electric current pulse (ECP) in an annealed Cu−40%Zn alloy was thoroughly investigated. The ECP induced β precipitates formed in the annealed α matrix follow different ORs depending on the formation site. At the α grain boundaries or their vicinities, the K-S OR is respected, whereas in the α grain interiors, the N-W OR is obeyed. In the former locations, $\{111\}_\alpha/<1\bar{1}0>_\alpha$ dislocation arrays are frequently observed, whereas in the latter stacking faults boarded with $\{111\}_\alpha/<11\bar{2}>_\alpha$ partial dislocations are often spotted. Analysis of the transformation lattice deformation revealed that under the different ORs, the lattice strain to realize the structure change for the α to β transformation is different. For the K-S strain path, the principal resistance is the shear strain on the $\{111\}_\alpha$ plane and in the $<1\bar{1}0>_\alpha$ direction, whereas for the N-W path, the principal obstacle is the shear on the $\{111\}_\alpha$ plane and in the $<11\bar{2}>_\alpha$ direction. Thus the existing $\{111\}_\alpha/<1\bar{1}0>_\alpha$ dislocation arrays provide the favorable pre-strains to facilitate the formation of the β precipitates via the K-S path. The

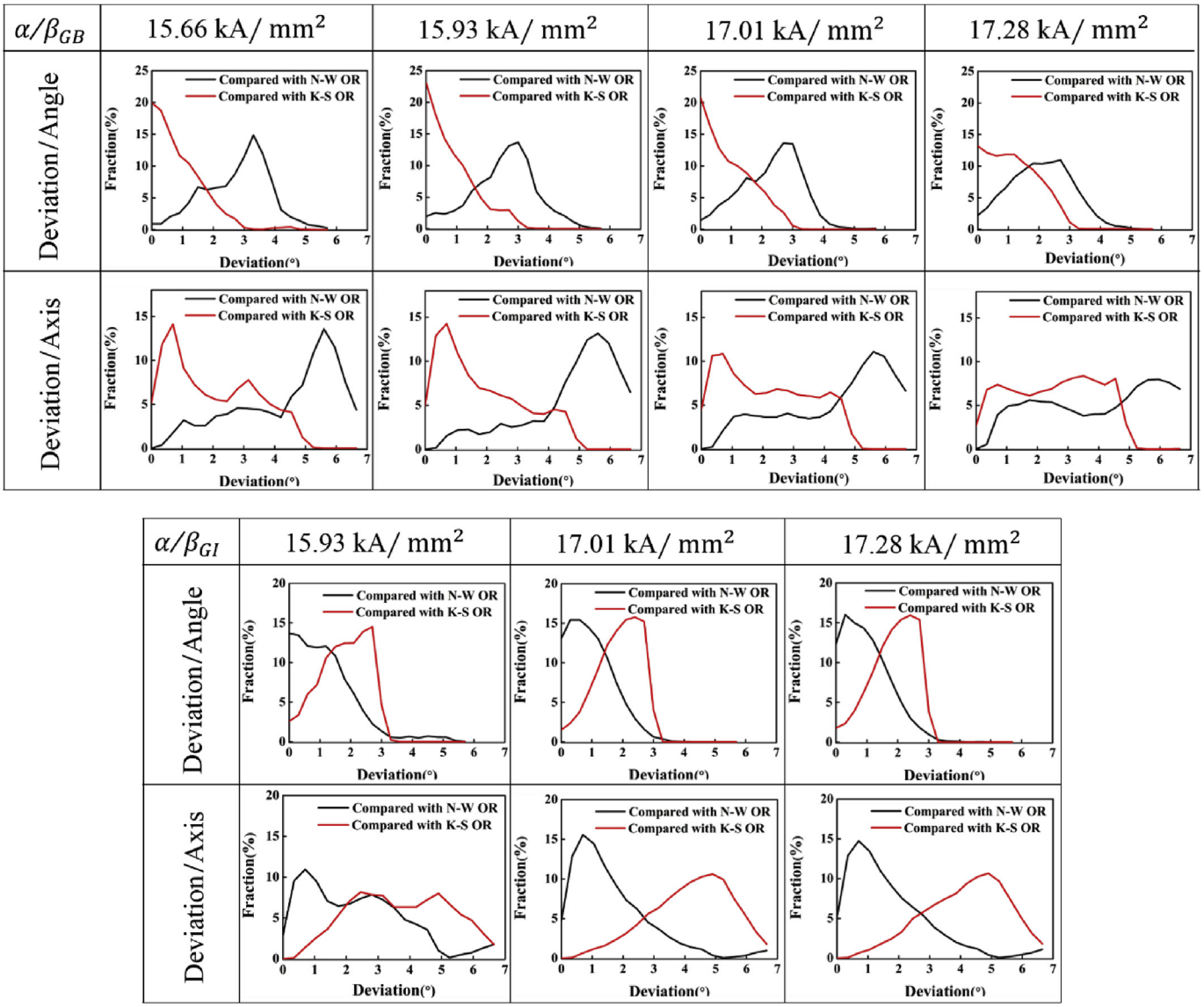

Fig. 7. Variations of β/α phase boundary length fractions of all the selected β_{GB} and β_{GI} with the deviations from the ideal N-W OR (equivalent to a 45.98° rotation around the <0.976 0.083 0.201 > axis) (in black) and also from the ideal K-S OR (equivalent to a 42.85° rotation around the <0.968 0.178 0.178 > axis) (in red) under different ECP treatments. The deviations are both from the rotation angle and the rotation axis. For the β_{GI}, the statistics were counted from about 500 precipitates at 15.93 kA/mm^2 to 2000 precipitates at 17.28 kA/mm^2 and for the β_{GB}, the statistics were collected from around 600 precipitates. (For interpretation of the references to color in this figure legend, the reader is referred to the Web version of this article.)

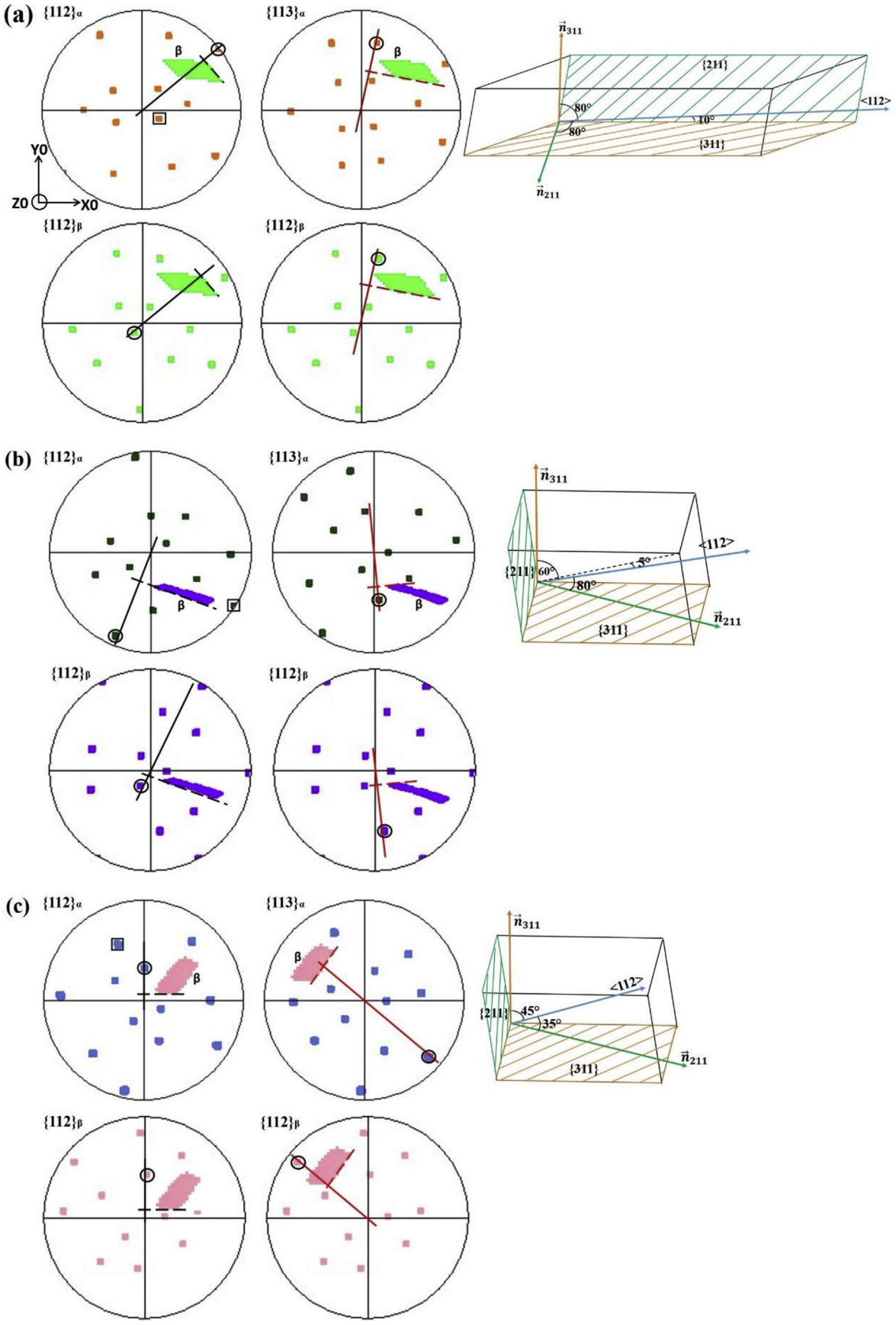

Fig. 8. $\{112\}_\alpha$ and $\{113\}_\alpha$ pole figures of α phase possessing the three types of β precipitates (A, B and C) and their three-dimensional illustrations. (a) Precipitate Type A, (b) Type B and (c) Type C. The dash lines outline the surface plane traces of the precipitates and the solid lines connect the center of the pole figures with the poles corresponding to the surface planes and perpendicular to the surface plane traces with the same color. (For interpretation of the references to color in this figure legend, the reader is referred to the Web version of this article.)

Table 4
The geometrical relations between the OR direction $<112>_\alpha$ and the surface planes of the three types of precipitates (A, B and C) described with the angles between this direction and the corresponding surface plane normal directions $\vec{n}$.

	$<112>_\alpha$ Λ Shear Direction	$<112>_\alpha$ Λ $\vec{n}_{\{112\}_\alpha}$	$<112>_\alpha$ Λ $\vec{n}_{\{113\}_\alpha}$	Shape
A	10°	80°	80°	Long Bar
B	5°	80°	60°	Short Bar
C	10°–90°	10°–90°	10°–90°	Irregular

Table 5
The number percentage of the three types of β_{GI} obtained in different current density treatments.

Electric Current Density (kA/mm^2)	A	B	C
15.93	79.59%	8.16%	12.24%
17.01	72.46%	19.32%	8.21%
17.28	57.91%	20.89%	21.20%

existing $\{111\}_\alpha/<11\bar{2}>_\alpha$ stacking faults offer the favorable pre-strains for the formation of the β precipitates via the N-W path, resulting in the selection of ORs for the α to β transformation.

With the present work, the correlation between the types of existing crystal defects (dislocations and stacking faults) and the transformation orientation relationships was confirmed. The roles of different dislocations in providing favorable pre-strain to contribute to the transformation strain process of the α to β transformation under different ORs were fully revealed. The methodology of the present work is applicable to phase transformations in many other metallic materials.

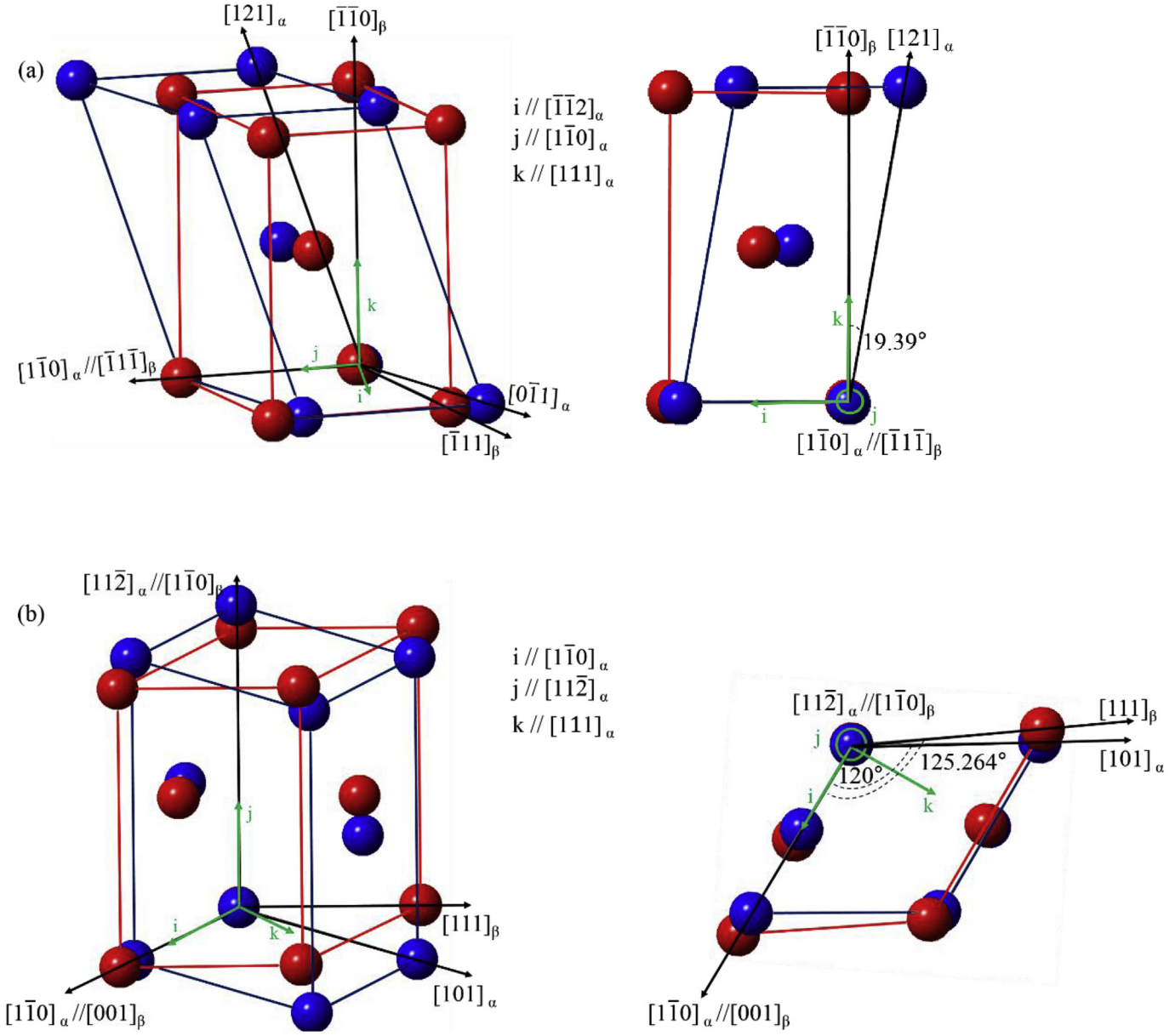

Fig. 9. Lattice correspondences between α and β under the K-S (a) and under the N-W OR (b). The OR reference systems (*i*-*j*-*k*) are set with direction *j* parallel to the OR direction, *k* to the direction normal to the OR plane and *i* to the vector cross product of *j* and *k*. The lattice points of the α are in blue and those of the β phase in red. (For interpretation of the references to color in this figure legend, the reader is referred to the Web version of this article.)

Table 6
Deformation gradient tensor of the structure deformation to form the β precipitates in the sample treated under j = 17.28 kA/mm^2 under the K-S and under the N-W OR expressed in the K-S and the N-W OR reference frame, respectively.

OR	Deformation Gradient Tensor
K-S	$i\|\|[\bar{1}\bar{1}2]\ j\|\|[1\bar{1}0]\ k\|\|[111]$ $\begin{bmatrix} 1.0634 & 0 & 0.1880 \\ -0.1880 & 0.9767 & 0.2658 \\ 0 & 0 & 0.9767 \end{bmatrix}$
N-W	$i\|\|[1\bar{1}0]\ j\|\|[11\bar{2}]\ k\|\|[111]$ $\begin{bmatrix} 1.1279 & 0 & 0 \\ 0 & 0.9209 & 0.3256 \\ 0 & 0 & 0.9767 \end{bmatrix}$

Acknowledgements

This work was supported by the 111 Project of China (Grant No. B07015), and the National Nature Science Foundation of China, Grant No. 51471047, the Fundamental Research Funds for the Central Universities No. N130418001. The first author Meishuai Liu is grateful to the China Scholarship Council for the support to her PhD study in France.

References

[1] W. Gong, Y. Tomota, Y. Adachi, A.M. Paradowska, J.F. Kelleher, S.Y. Zhang, Effects of ausforming temperature on bainite transformation, microstructure and variant selection in nanobainite steel, Acta Mater. 61 (2013) 4142–4154.
[2] N. Yoshinaga, H. Inoue, K. Kawasaki, L. Kestens, B.C. De Cooman, Factors affecting texture memory appearing through α→ γ→ α transformation in IF steels, Mater. Trans. 48 (2007) 2036–2042.
[3] Y.L. He, S. Godet, P.J. Jacques, J.J. Jonas, Crystallographic features of the γ-to-α transformation in a Nb-added transformation-induced plasticity steel, Metall. Mater. Trans. A 37 (2006) 2641–2653.
[4] H.Y. Song, H.T. Liu, G.D. Wang, J.J. Jonas, formation of widmanstätten austenite in strip cast grain-oriented silicon steel, Metall. Mater. Trans. A 48 (2017) 1959–1968.
[5] L. Bracke, L. Kestens, J. Penning, Transformation mechanism of α′-martensite in an austenitic Fe–Mn–C–N alloy, Scripta Mater. 57 (2007) 385–388.
[6] T. Watanabe, K. Obara, S. Tsurekawa, G. Gottstein, A mechanism of plane matching boundary-assisted α/γ phase transformation in Fe–Cr alloy based on in-situ observations, Z. Metallkd 96 (2005) 1196–1203.
[7] L. Kestens, R. Petrov, Y. Houbaert, Orientation selective martensite transformation in an Fe-28Ni alloy, ISIJ Int. 43 (2003) 1444–1452.
[8] N. Stanford, P.S. Bate, Crystallographic variant selection in α–β brass, Acta Mater. 53 (2005) 859–867.
[9] B. Gabriele, A. Köntges, G. Gottstein, Microstructure and texture development during the phase transformation in an Fe-Ni-Co-Ti shape memory alloy, Steel Res. Int. 70 (1999) 188–192.
[10] Y.L. He, S. Godet, P.J. Jacques, J.J. Jonas, Crystallographic relations between face-and body-centred cubic crystals formed under near-equilibrium conditions: observations from the Gibeon meteorite, Acta Mater. 54 (2006) 1323–1334.
[11] S.M.C. van Bohemen, A. Kamp, R.H. Petrov, L.A.I. Kestens, J. Sietsma, Nucleation and variant selection of secondary α plates in a β Ti alloy, Acta Mater. 56 (2008) 5907–5914.
[12] G.H. Cao, A.M. Russell, C.G. Oertel, W. Skrotzki, Microstructural evolution of TiAl-based alloys deformed by high-pressure torsion, Acta Mater. 98 (2015) 103–112.
[13] M. Bönisch, M. Calin, L. Giebeler, A. Helth, A. Gebert, W. Skrotzki, J. Eckert, Composition-dependent magnitude of atomic shuffles in Ti–Nb martensites, J. Appl. Crystallogr. 47 (2014) 1374–1379.
[14] M. Bönisch, T. Waitz, M. Calin, W. Skrotzki, J. Eckert, Tailoring the Bain strain of martensitic transformations in TiNb alloys by controlling the Nb content, Int. J. Plast. 85 (2016) 190–202.
[15] Z.B. Li, Y.D. Zhang, C. Esling, X. Zhao, L. Zuo, Determination of the orientation relationship between austenite and incommensurate 7M modulated martensite in Ni–Mn–Ga alloys, Acta Mater. 59 (2011) 2762–2772.
[16] Z.B. Li, B. Yang, Y.D. Zhang, C. Esling, N.F. Zou, X. Zhao, L. Zuo, Crystallographic insights into the intermartensitic transformation in Ni–Mn–Ga alloys, Acta Mater. 74 (2014) 9–17.
[17] D. De Knijf, T. Nguyen-Minh, R.H. Petrov, L.A.I. Kestens, J.J. Jonas, Orientation dependence of the martensite transformation in a quenched and partitioned steel subjected to uniaxial tension, J. Appl. Crystallogr. 47 (2014) 1261–1266.
[18] J.J. Jonas, Y.L. He, S. Godet, The possible role of partial dislocations in facilitating transformations of the Nishiyama–Wassermann type, Scripta Mater. 52 (2005) 175–179.
[19] N.J. Wittridge, J.J. Jonas, J.H. Root, A dislocation-based model for variant selection during the γ-to-α transformation, Metall. Mater. Trans. A 32 (2001) 889–901.
[20] H.J. Bunge, W. Weiss, H. Klein, L. Wcislak, U. Garbe, J.R. Schneider, Orientation relationship of Widmannstätten plates in an iron meteorite measured with high-energy synchrotron radiation, J. Appl. Crystallogr. 36 (2003) 137–140.
[21] Y.Z. Zhou, W. Zhang, J.D. Gou, G.H. He, Diffusive phase transformation in a Cu-Zn alloy under rapid heating by electropulsing, Phil. Mag. Lett. 84 (2004) 341–348.
[22] Y.Z. Zhou, W. Zhang, B.Q. Wang, G.H. He, J.D. Gou, Grain refinement and formation of ultrafine-grained microstructure in a low-carbon steel under electropulsing, J. Mater. Res. 17 (2002) 2105–2111.
[23] X.L. Wang, Y.B. Wang, Y.M. Wang, B.Q. Wang, J.D. Guo, Oriented nanotwins induced by electric current pulses in Cu-Zn alloy, Appl. Phys. Lett. 91 (2007), 163112.
[24] Y.Z. Zhou, J.D. Gou, W. Zhang, G.H. He, Influence of electropulsing on nucleation during phase transformation, J. Mater. Res. 17 (2002) 3012–3014.
[25] W. Zhang, W.S. Zhao, D.X. Li, M.L. Sui, Martensitic transformation from α-Ti to β-Ti on rapid heating, Appl. Phys. Lett. 84 (2004) 4872–4874.
[26] Y. Jiang, G. Tang, C. Shek, Y. Zhu, Z. Xu, On the thermodynamics and kinetics of electropulsing induced dissolution of β-Mg17Al12 phase in an aged Mg–9Al–1Zn alloy, Acta Mater. 57 (2009) 4797–4808.
[27] A.F. Sprecher, S.L. Mannant, H. Conrad, On the mechanisms for the electroplastic effect in metals, Acta Metall. 34 (1986) 1145–1162.
[28] H. Conrad, Effects of electric current on solid state phase transformation in metal, Mater. Sci. Eng., A 287 (2000) 227–237.
[29] Y. Dolinsky, T. Elperin, Thermodynamics of phase transitions in current-carrying conductors, Phys. Rev. B 47 (1993) 14778–14785.
[30] Y. Dolinsky, T. Elperin, Thermodynamics of nucleation in current-carrying conductors, Phys. Rev. B 50 (1994) 52–58.
[31] R.S. Qin, B.L. Zhou, Effects of electric current pulses on grain size in castings, Int. J. Non Equilib. Process. 11 (2004) 77–86.
[32] X.L. Wang, M.S. Liu, W.B. Dai, X. Nan, X. Zhao, Effect of electric current direction on the microstructural evolution and mechanical properties of a cold-rolled Cu-Zn alloy during the phase transformation induced by electric current pulses, J. Mater. Res. 30 (2015) 2500–2507.
[33] X.L. Wang, W.B. Dai, R. Wang, X.Z. Tian, X. Zhao, Enhanced phase transformation and variant selection by electric current pulses in a Cu-Zn alloy, J. Mater. Res. 29 (2014) 975–979.
[34] M.S. Liu, X.L. Wang, X. Zhao, Effect of high-density electric current pulses on precipitation and mechanical properties of a Cu–Zn alloy, Mater. Sci. Technol. (2017) 1–6.
[35] B. Beausir, J.-J. Fundenberger, ATEX - Software, Analysis Tools for Electron and X-ray Diffraction, Université de Lorraine, Metz, 2017. www.atex-software.eu.
[36] J.-J. Fundenberger, A. Morawiec, E. Bouzy, J.-S. Lecomte, Polycrystal orientation maps from TEM, Ultramicroscopy 96 (2003) 127–137.
[37] A. Morawiec, J.-J. Fundenberger, E. Bouzy, J.-S. Lecomte, EP—a program for determination of crystallite orientations from TEM Kikuchi and CBED diffraction patterns, J. Appl. Crystallogr. 35 (2002), 287–287.
[38] Y.D. Zhang, S.Y. Wang, C. Esling, J. Lecomte, C. Schuman, X. Zhao, L. Zuo, A method to identify dislocations in a known crystal structure by transmission electron microscopy, J. Appl. Crystallogr. 44 (2011) 1164–1168.
[39] Crystal Maker software, http://www.crystalmaker.com.